Nuclear Instruments and Methods in Physics Research A274 (1989) 79–94
North-Holland, Amsterdam



# $e^+e^-$ POLARIMETRY AT LEP

M. PLACIDI [1] and R. ROSSMANITH [2]

[1] *CERN, CH-1211 Geneva 23, Switzerland*
[2] *CEBAF, Newport News, Virginia 23606, USA*

Received 12 July 1988

The design of a fast Compton-scattering laser polarimeter for LEP is outlined. Although the design is optimized for LEP at 50 GeV/beam, general considerations are extended to LEP energies up to 100 GeV/beam.

Besides a recall of the physics of the polarimeter the study includes considerations on the background and consequent design of the layout, the optimization of the laser–electron beam interaction region, the specifications of the laser to fit the LEP energy range and an overview of the devices to be used as detectors for the high energy backscattered γ-beam.

A 50% polarization level is expected to be measured in a few seconds with an accuracy of about 3%.

## 1. Introduction

The current knowledge of the problems connected with polarization in LEP [1] suggests good and fast polarimetry as an essential tool for implementing orbit correction strategies to obtain polarized beams. Following early investigations on the possibility of achieving polarized beams in LEP [2,3] a detailed study of a laser polarimeter for LEP is presented. The feasibility considerations described in previous reports [4,5] are developed in a proposal containing the specifications to meet these requirements.

The initial task will be to measure and to optimize the transverse polarization and to provide useful information for the future plans for longitudinally polarized beams in LEP. This polarimeter also allows for the measurement of longitudinal polarization if required; the extension of this device to a longitudinal polarimeter is considered in detail in [6].

The feasibility study is carried on with the aim of measuring the degree of polarization of both the electron and the positron beams in LEP. The depolarizing effects experienced by the two beams can in fact be different mainly due to orbit offsets in quadrupoles connected with distributed machine errors and unsymmetrically excited rf cavities. For simplicity of notation it is assumed in the text that the laser interacts with the electron beam but all the technical considerations can be adopted for the measurement of the polarization of both beams.

After a short review of the polarization mechanisms in $e^{\pm}$ storage rings with special reference to LEP, the principles of operation of the laser polarimeter are recalled and the applications to LEP Phase I considered. Background considerations leading to the choice of the layout and a detailed analysis of the interaction between the laser and the particle beam, together with its influence on the design of the interaction region, are presented. The influence of the laser parameters on the design has been investigated to optimize the performance of the polarimeter.

Account is finally given for the expected rates and the required acquisition time to measure the degree of polarization within a given accuracy.



## 2. Polarization in LEP

### 2.1. The natural radiative polarization

Considering the natural radiative Sokolov–Ternov mechanism [7] from the guiding magnetic field and the depolarizing effects originating from radial fields in a real storage ring (misalignments, c.o. distortions etc.) the buildup of the polarization can be described by an exponential behaviour [8]:

$$P_e(E, t) = \frac{\pm P_{max}(1 - e^{-t/\tau})}{1 + \tau_p/\tau_d}, \qquad (1)$$

where

$\pm P_{max}$ is the Sokolov–Ternov asymptotic polarization level,

$1/\tau = 1/\tau_p + 1/\tau_d$ is the effective buildup constant,

$\tau_p(E)$ is the natural radiative polarization rise time, and,

$\tau_d$ describes the effect of the depolarizing mechanisms.

The $\pm$ sign (+ for positrons) accounts for the spin orientation with respect to the magnetic moment.

The beam polarization (1) can be expressed in terms of the measurable constant time $\tau$ as

$$P_e(E, t) = +(\tau/\tau_p) P_{max}(1 - e^{-t/\tau}). \quad (1')$$

### 2.2. Polarization enhancement

For storage rings having a "regular" lattice the ideal radiative asymptotic level $P_{max}$ and the rise time $\tau_p$ are given by the relations

$$P_{max} = 8/(5\sqrt{3}) = 92.38\%,$$
$$\tau_p = 1.63(R/\rho)(\rho^3/E^5) \quad [\text{min}], \quad (2)$$

where $R$ is the machine average radius and $\rho$ the dipole bending radius.

In LEP Phase I the natural radiative polarization time without wigglers would be quite long:

$$\tau_p = 6.64/(E/100)^5 \rightarrow 5.5 \text{ h at } 46 \text{ GeV}, \quad (3)$$
$$\rightarrow 1.4 \text{ h at } 60 \text{ GeV}.$$

To reduce the natural polarization time for large $e^\pm$ storage rings asymmetric (dipole or multipole) wigglers have been suggested [9–12].

Eight asymmetric dipole wiggler magnets [13] are foreseen to control the LEP beam characteristics such as emittance, energy spread, damping and polarization times. The modified values of the asymptotic polarization level and of the polarization time, evaluated [14] for the situation where all wigglers are excited to their maximum field, are, in the LEP energy range 46 to 55 GeV,

$$(P_{max})_w \approx 73\text{–}78\%,$$
$$(\tau_p)_w \approx 90\text{–}50 \text{ min}. \quad (2')$$

A new generation of wigglers has been proposed recently [15] which reduces even more the polarization time ($\tau_p \approx 36$ min around 46 GeV), without penalizing the asymptotic value.

## 3. The laser polarimeter

Originally suggested by Baier and Khoze [16], the laser polarimeter has become a part of the standard equipment in $e^\pm$ storage rings above 1 GeV. The first example of this kind of apparatus worked at SPEAR [17] and since then almost all the accelerator laboratories operating with $e^\pm$ storage rings have adopted the laser polarimeter as a powerful diagnostics tool [18–22].

The laser polarimeter is based on spin dependent Compton scattering of circularly polarized photons from a high energy electron/positron beam. The backscattered $\gamma$-rate is given by

$$\dot{n}_\gamma = \mathcal{L}\sigma_c(P_e, P_\phi), \quad (4)$$

where

$$\mathcal{L} = f\frac{N_e N_\phi}{\Sigma} \quad (5)$$

is the luminosity of the electron beam-laser interaction, $f$ the laser repetition rate, $N_e$ the electron bunch charge, $N_\phi$ the laser pulse intensity and $\Sigma$ the interaction area.

The spin-dependent total Compton cross section $\sigma_c(P_e, P_\phi)$ has been calculated by Lipps and Toelhoek [23] and is briefly recalled in Appendix A [eq. (A.1)]. The notation for the kinematics in the electron rest frame and in the laboratory system are those of fig. 1. For photon energies small compared with the electron rest mass this formula can be integrated. The behavior of $\sigma_c(P_e, P_\phi)$ is shown in fig. 2 as a function of $\vartheta'$ for $P_e$ and $P_\phi = 100\%$. Curve a) represents the cross section for 46 GeV unpolarized electron beams; curves b) and c) refer to polarized beams illuminated by left- and right-hand circularly polarized laser light.

The backscattered high energy $\gamma$-rays travel towards a detector which records their vertical angular distribu-

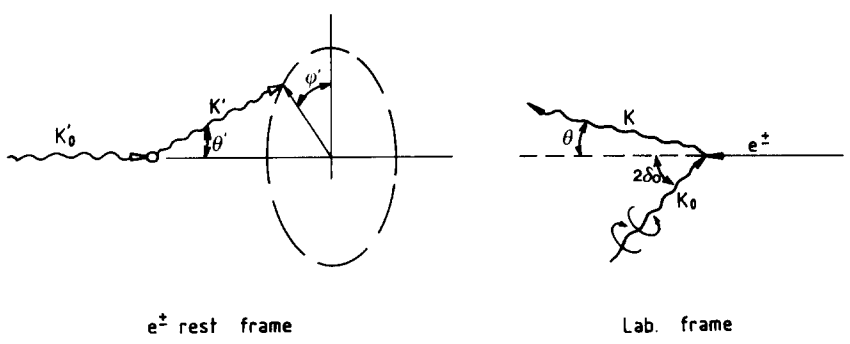


Fig. 1. Notation for Compton kinematics.

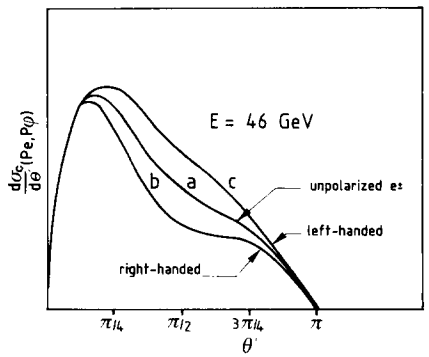


Fig. 2. Spin-dependent Compton cross section vs scattering angle $\vartheta'$. a) unpolarized 46 geV electrons. b) right- and c) left-handed circularly polarized light on polarized electrons.

tion. If the electron beam is transversally polarized an up–down asymmetry in the γ-rate is present and two vertically shifted distributions result, depending on the left–right photon polarization. The electron polarization level is measured through the vertical asymmetry

$$A(y) = \frac{n_R - n_L}{n_R + n_L}, \tag{6}$$

where $n_R(y)$ and $n_L(y)$ are the γ-rates at a vertical position $y$ for the two photon helicities.

Introducing the cross section $\sigma_c(P_e, P_\phi)$ in the electron restframe the asymmetry (6) can be written

$$A(P_e, P_\phi) = \frac{(d\sigma/d\Omega)_R - (d\sigma/d\Omega)_L}{(d\sigma/d\Omega)_R + (d\sigma/d\Omega)_L} = \frac{\Phi_2}{\Phi_0} = P_e P_\phi \cos\phi' \, F(\vartheta', k_0'). \tag{7}$$

For a given kinematic situation defined by the angle $\vartheta'$ the function

$$F(\vartheta', k_0') = \frac{k' \sin\vartheta'(1-\cos\vartheta')}{1+\cos^2\vartheta' + (k_0' - k')(1-\cos\vartheta')} = \frac{\Phi_2(\phi'=0)}{P_e P_\phi \Phi_o} \tag{8}$$

is proportional to the incoming photon energy $E_\phi$ through the term $k_0'$ [eqs. (A.2) and (B.3)]

$$k_0' \approx 2\gamma k_0 = 2\gamma E_\phi / m_0 c^2, \tag{9}$$

where γ is the relativistic factor. The quantity $F$ as a maximum around $\vartheta' = \pi/2$ and thus the strongest spin dependence occurs for angles in the laboratory system $\vartheta \approx 1/\gamma$ [eq. (B.2)]. The dependence of the function $F$ (asymmetry for 100% photon and electron polarization) on the scattering angles $\vartheta$ and $\vartheta'$ is shown in fig. 3.

Two different methods can be adopted to illuminate the electron beam. In the *single-photon method* the beam is made to interact with the photons produced by a low energy, high repetition frequency laser pulse. The backscattered γ-rate per interaction is of the order of $\approx 1$ Hz and the maximum rate is then given by the revolution frequency of the electron bunch. The *multi-photon technique* adopts a high peak power laser to produce at least $10^4$ γ's per interaction. In this case the maximum γ-rate is limited by the laser repetition rate but the method provides a much more efficient background rejection.

## 4. Measurements and monitoring

### 4.1. Relative measurements

Absolute beam energy calibration will be the first application of polarimetry at LEP. The experimental

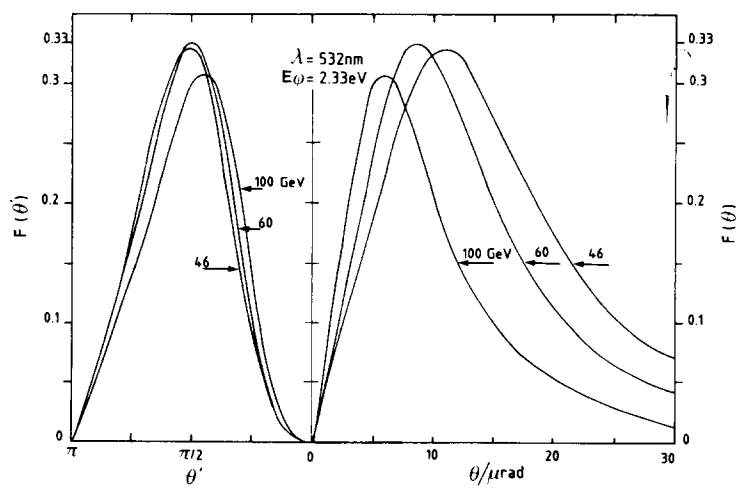


Fig. 3. Asymmetry vs scattering angles $\vartheta'$ and $\vartheta$ for 100% photon and electron polarization.

evidence of some beam polarization and the record of the associated asymmetry from the polarimeter data can in fact be used as a refined method to precisely calibrate the average energy of a storage ring through an induced spin resonance.

A depolarizer device [24] generating an rf radial magnetic field is used to induce a spin resonance on the circulating beam without perturbing the machine operation. Changes in the $\gamma$-rate asymmetry are monitored as a function of the driving frequency and the average machine energy can be determined to the accuracy of the electron rest mass since the $e^{\pm}$ gyromagnetic anomaly

$$a(e^{\pm}) \equiv (g-2)/2 = 1159652188 \times 10^{-12} \qquad (10)$$

is known to a precision of some $10^{-9}$ [25].

The same method can be adopted to monitor the actual machine energy in conjunction with experimental data taking to allow for precise measurements of particle masses [18–20]. In this case special care has to be taken to compensate the depolarizing effects of the experimental solenoids. Other machine parameters can be measured in an absolute way through relative asymmetry measurements [26].

### 4.2. Absolute measurements

a) The absolute value of the asymptotic degree of polarization (1) can be determined by measuring the time dependence of the asymmetry (6) and deriving the effective rise time $\tau_x$ by a least squares fit to the experimental points [27]. The real asymptotic polarization level is then

$$P_\infty(E) \equiv P(E, t \to \infty) = \tau_x \left(P_{max}/\tau_p\right)_w. \qquad (11)$$

The actual values for $P_{max}$ and $\tau_p$ are to be scaled from (2′) according to the real fraction of wiggler power adopted during the measurements.

b) The absolute measurement of the attainable transverse polarization level will be of extreme interest to verify the possibilities of overcoming the depolarization problems in the 50 GeV energy range and will influence the future plans for providing longitudinal polarization at LEP. The absolute value of the electron polarization can be derived from the measured $\gamma$-rate asymmetry $A$:

$$P_e = A/\Pi P_\phi, \qquad (12)$$

where the analyzing power $\Pi$ is calculated from the theory and averaged over the kinematic region defined by the angular acceptance of the detector.

### 4.3. Monitoring

Circularly polarized light is generated by inserting a $\lambda/4$-wave plate on the original linearly polarized laser beam. Left- and right-handed polarization light is then obtained by rotating by $\pm 90°$ the $\lambda/4$ plate. The photon helicity has to be changed rather often during data taking to average out false asymmetries coming from drifts in the closed orbit slope at the interaction region.

The quality of the photon circular polarization might be affected by the optical elements in the transport line and in particular by birefringence in the windows. This effect cannot be numerically quantified and has to be studied in the laboratory prior to the installation of the apparatus.

The effective circular polarization $P_\phi$ of the laser beam at LIR has to be properly measured if the absolute polarization of the electron beams is aimed at. Two methods can be considered. In the SLC proposal [22] the light is reflected back by a retromirror located beyond the interaction point and its polarization is measured in the laser shack. As an alternative we envisage a "remote polarimetry" on the light recuperated after the interaction, near the vacuum insertion.

Synchronization of the laser pulse is not very critical if most error comes from the time jitter ($\approx 0.25$ ns for a 6–7 ns rms pulse duration, see table 4). The short electron bunchlength ($\approx 60$ ps rms) and the reduced interaction angle allow for a complete longitudinal overlap of the two distributions so the jitter has to be compared to the interaction length which is governed by the laser pulse duration. The influence of this parameter on the luminosity of the Compton interaction is discussed in section 8.2.

## 5. Background considerations

The background will consist of two components: gas bremsstrahlung and synchrotron radiation. In the following the background conditions in the straight section LSS1 are investigated to optimize the polarimeter layout.

### 5.1. Gas bremsstrahlung

The total cross section $\sigma_{gb}$ [mb] for the gas bremsstrahlung can be found in [28]. The parameter is the ratio $\epsilon_s = k/E$ between the photon and the electron energies.

$$\sigma_{gb}(\epsilon_s) = 57.3\left\{6.37\left[\epsilon_s - \ln(\epsilon_s)\right] - 2.34\epsilon_s^2 - 4.03\right\}. \qquad (13)$$

The rate of bremsstrahlung photons from 1 mA bunch on the residual gas in LSS1 with $\langle Z \rangle = 5$, average pressure $= 5 \times 10^{-9}$ Torr, path length $= 500$ m and $\epsilon_s \geq 0.2$ is of the order of two photons per interaction.

Table 1
Flux of synchrotron radiation photons with energies higher than 0.5 MeV emitted from the magnetic elements in LSS1 at 55 GeV [a]

| Source | $\rho$ (km) | $\epsilon_c$ (keV) | $N_d$ ($10^{12}$ ph $mA^{-1}s^{-1}$) | $P_d$ (GeV/crossing) |
|---|---|---|---|---|
| Main dipole | 3.096 | 120 | 4 | $1.4\times10^{5}$ |
| 10% dipole | 30.96 | 12 | $5.6\times10^{-17}$ | $2\times10^{-12}$ |
| Quadrupoles | $\approx 10$ | $\leq 40$ | $\leq 1.5\times10^{-3}$ | $\approx 50$ |
| Corr. dipoles | | | | |
| 100% | 2 | 184 | 220 | $7.5\times10^{6}$ |
| 50% | 4 | 92 | 5.2 | $2\times10^{5}$ |
| 30% | 6.7 | 55 | 0.07 | $2\times10^{3}$ |
| Miniwigglers | 0.877 | 420 | $10^{3}$ | $3.6\times10^{7}$ |

[a] Arc trajectories of 1 m (main dipole), 10 m (10% dipole), 2 m (both miniwigglers), 6.5 m (16 c.o. correctors) and 24 m (24 quadrupoles) are considered as contributing to the synchrotron radiation background within the detector acceptance.

### 5.2. Synchrotron radiation

The situation in LEP is different from other machines. The critical energy of the radiation produced in the main dipoles ($\approx 120$ keV at 55 GeV) is already in the range where the attenuation of photons by matter is more or less energy independent [29]. As a consequence a shield acts in the same way both on synchrotron radiation and backscattered photons.

A formula giving the number $N_{sr}$ of (photons/s) (mA/m) emitted above a certain energy $u$/keV as a function of the energy $E$ and the bending radius $\rho$ is given in [30]:

$$N_{sr} = 4.6\times10^{16}\exp(-0.45\,u\rho/E^3)\sqrt{E^5/u\rho^3}. \qquad (14)$$

Four main sources of synchrotron radiation in LSS1, namely the standard dipole magnets, the normal conducting quadrupoles, the orbit correctors and the miniwiggler system [31] are compared with the 10% dipole. The results are collected in table 1 for $E = 55$ GeV and $u = 500$ keV.

In any possible experimental arrangement a number $N_d = \int N_{sr}\,dl$ of photons generated along trajectories of either $\approx 1$ m in the bending magnets or of $\approx 2$ m in the miniwigglers would fall into the detector. A lower limit for the synchrotron radiation deposition in the detector can be computed by assuming that all the photons have the same energy $u$. The deposited power for $I = 3$ mA/beam is then

$$P_d = uIN_d = \begin{cases} 6\times10^{9}\ \text{GeV/s} \rightarrow \\ \quad 1.4\times10^{5}\ \text{GeV/crossing} \\ \quad \text{(dipole)}, \\ 1.6\times10^{12}\ \text{GeV/s} \rightarrow \\ \quad 3.6\times10^{7}\ \text{GeV/crossing} \\ \quad \text{(miniwiggler)}. \end{cases} \qquad (15)$$

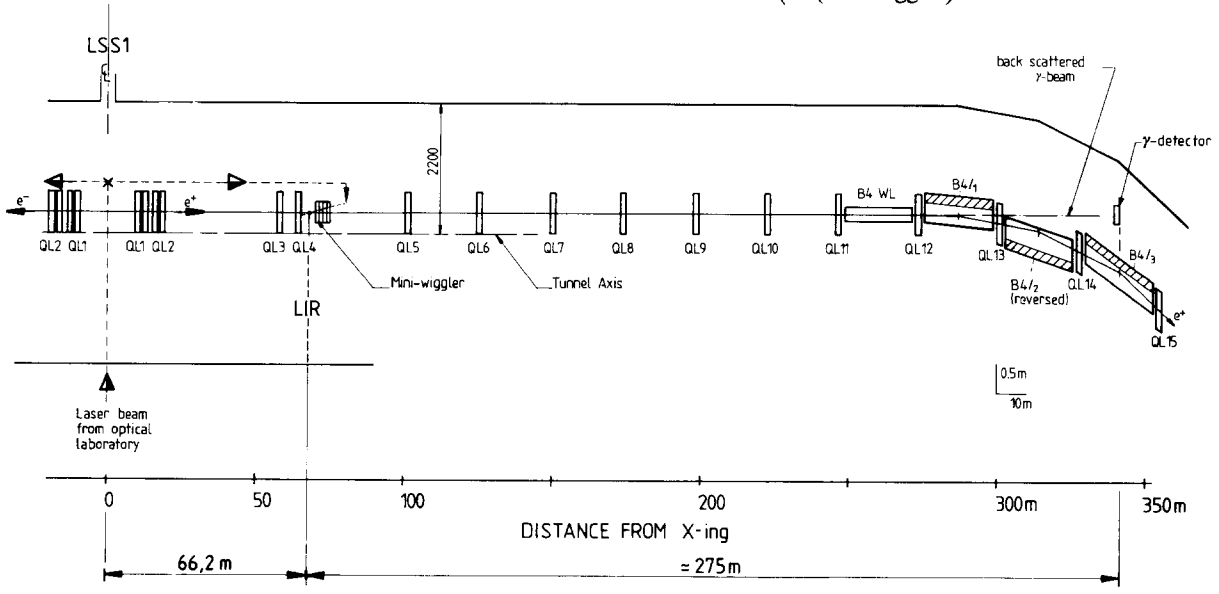


Fig. 4. General layout of the LEP polarimeter for positrons in LSS1.

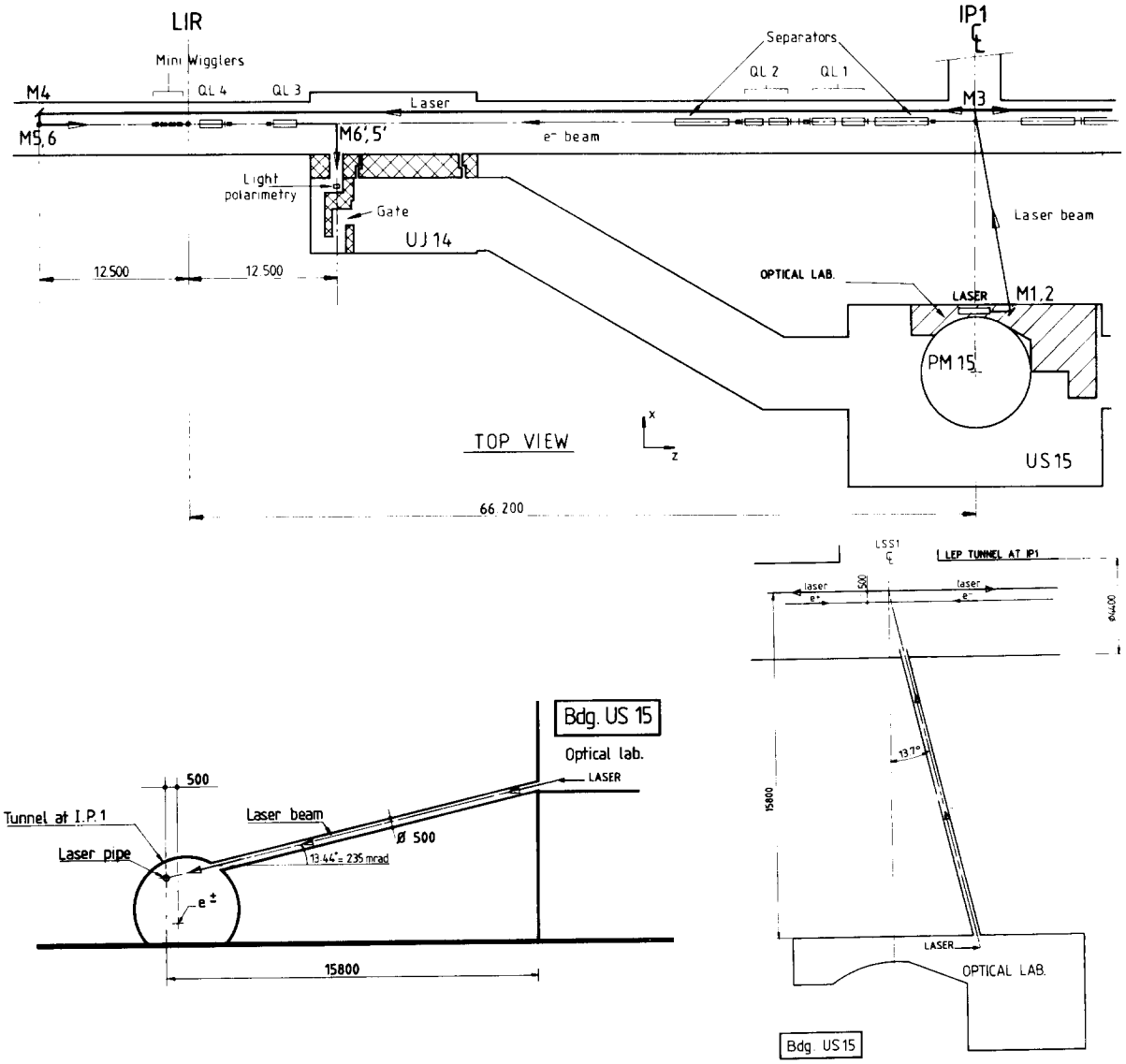


Fig. 5. Connections between Optical Laboratory and LSS1 straight section in LEP tunnel.

The radiation emitted by the closed orbit correctors [32] must be carefully considered. According to the results collected in table 1 the 16 correction dipoles in LSS1 should not be powered, if all used at the same time, to more than $\approx 30\%$ of their maximum. The contribution from the 24 quadrupoles in LSS1 has also been estimated assuming the full bunch charge travelling along all of them with a $\pm 2.6$ mm offset (i.e. $\pm 1\sigma$ at maximum $\beta$ function).

Figures collected in table 1 have to be compared with the energy deposited by the recoil $\gamma$-beam. Assuming that $\approx 1$ recoil $\gamma$ per interaction is emitted with an energy of $\approx 25$ GeV in the *single-photon method*, the deposited energy is $\approx 25$ GeV/crossing and with four bunches/beam the maximum $\gamma$-rate would be about 45 kHz. If $\approx 10^4$ $\gamma$'s per interaction are produced in an average energy range of 25 GeV with the *multiphoton technique* the deposited energy is $\approx 2.5 \times 10^5$ GeV/crossing. Even adopting the multiphoton technique the synchrotron radiation background from the main dipoles would be at least 6 times the signal. As a consequence the layout described in section 6 has been proposed. The operation of the polarimeters is then only incompatible with the miniwigglers which shall not be used in conjunction with polarization measurements.

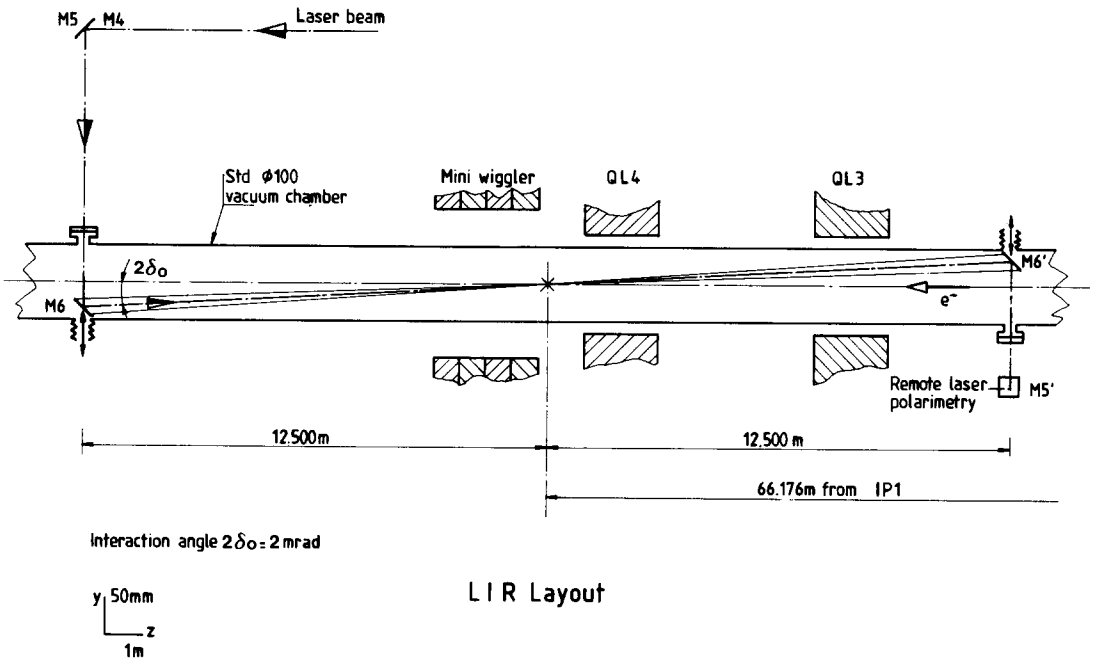


Fig. 6. Layout of the laser–electron interaction region (LIR).

## 6. Layout

According to the previous considerations the layout of fig. 4 has been adopted to prevent the synchrotron radiation from the main dipoles from hitting the detector *.

As shown in fig. 5, the photon beam produced by a laser installed in the Optical Laboratory (OL) in building US15 in front of IP1, is directed towards the LEP tunnel through a $\approx 14$ m long channel drilled in the rock. The light is then deflected towards the electron–laser interaction region (LIR) located between quadrupoles QL4 and QL5, where it interacts with the LEP beams (fig. 6). The Compton-backscattered $\gamma$'s travel along with the LEP beams up to the 10% dipole B4WL, leave the LEP vacuum chamber at the end of the first dipole B4/1 and after passing between the external coils of the quadrupole QL13 reach the $\gamma$-detector through a $\approx 40$ m long evacuated path (fig. 7). The detector is installed behind the dipole B4/3 at about 275 m from the LIR, $\approx 341$ m from IP1. Some modifications to the machine layout are required for the extraction of the recoil $\gamma$'s:

1) The dipole B4/2 and the orbit correcting dipole MCHA next to QL13 must be reversed.
2) The external coils of the quadrupole QL13 must provide a 20 mm vertical aperture.
3) The vacuum chamber in dipole B2R of B4/1 has to be enlarged.

* The synchrotron radiation emitted in the first normal bending magnet B4/1 does not hit the detector because of the 0.754 mrad deflection in the preceeding B4WL 10% dipole, the radiation of which can be neglected (section 5).

## 7. The laser beam and the interaction region

### 7.1. The illumination point

For a given electron polarization level the asymmetry (4) depends on the optical beam parameters at the illumination point and on its distance from the detector. The maxima for the asymmetry $A$ and the analyzing power $\Pi$ occur at a distance

$$L_{\text{opt}} = \beta/\alpha, \tag{16}$$

where $\alpha$ and $\beta$ are the beam Twiss parameters at the LIR. Considering the possible location for the detector

Table 2
Twiss parameters for the electron beam in the interaction region ($E = 55$ GeV, $\epsilon_h = 55.6$ nm, $\epsilon_v = 2.2$ nm)

| | LIR | | Mirror $M_6$ | |
|---|---|---|---|---|
| | II | V | H | V |
| $\alpha$ | −0.105 | 2.779 | −0.069 | 1.896 |
| $\beta$ [m] | 21.599 | 123.438 | 31.533 | 65.00 |
| $\sigma$ [mm] | 1.096 | 0.525 | 1.325 | 0.38 |
| $\sigma'$ [$\mu$rad] | 51.03 | 12.56 | 51.03 | 12.56 |

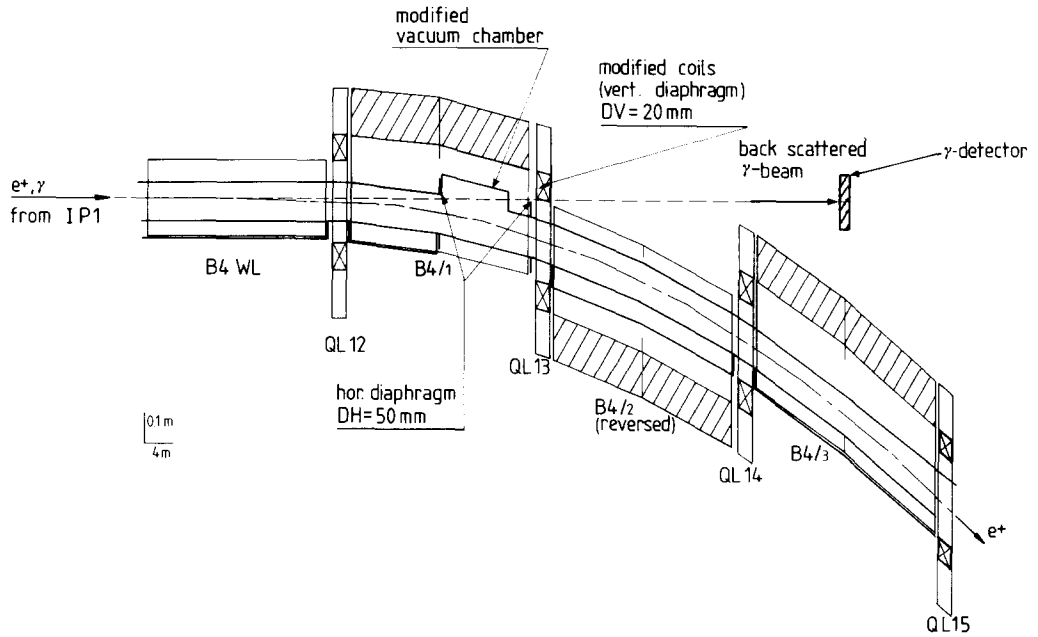


Fig. 7. Detail of the modified arc layout showing $e^+$ and γ-beam paths.

in the LEP tunnel the condition (16) could only be satisfied by illuminating the beam inside a vertically focusing quadrupole. Here the ratio $\beta/\alpha$ varies rapidly along the about 1 m long interaction region, while it is practically constant in a long drift space. From the above considerations the LIR has been located 1 m downstream the D-quadrupole QL4.

The asymmetry for the Twiss beam parameters at the interaction region collected in table 2 has been evaluated with the code ASYM [33,34] briefly described in [5] and the vertical beam profiles for both laser helicities are shown in fig. 8. The same exercise has been performed simulating a laser–beam interaction region inside QL4. to fulfill the relation (16). The two cases are compared in fig. 9. It can be seen that without any appreciable loss in the asymmetry, the distance between positive and negative maxima is about two times larger in the case a) (illumination point outside QL4) which is very useful to relax the vertical resolution of the detector.

### *7.2. The special vacuum insertion*

Experience at PETRA has shown that total internal reflection prisms used as last mirrors inside the vacuum chamber were seriously damaged by the high peak power laser beam in presence of synchrotron radiation. A possible explanation is the creation of "colour centres" in the prisms and consequent localized energy concentration up to densities dangerous for the stability of the structure.

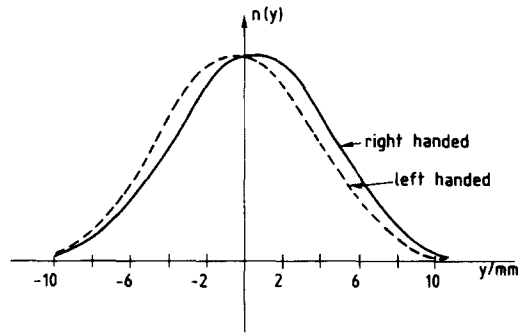


Fig. 8. Vertical beam profiles at the γ-detector.

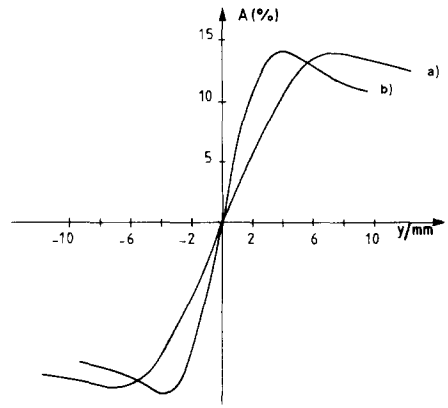


Fig. 9. Asymmetries at the γ-detector for two illumination points: a) LIR 1 m downstream QL4. b) LIR inside QL4.

Table 3
Laser beam optics at LIR

| | |
|---|---|
| Diffraction limited beam size at focus [mm] | 0.4 |
| Nominal beam size at focus [mm] | 2.4 |
| Full angle divergence at focus (max) [mrad] | $\leq 2.7$ |
| Nominal beam size at the optical systems (max) [mm] | $\leq 35$ |
| Final optical system aperture [mm] | 50 |
| Final optical system focal length [m] | 10.3 |
| Mirror $M_6$ size [mm$^2$] | $36 \times 50$ |
| Mirror to electron beam clearance [mm] | $\geq 10$ |
| Interaction angle [mrad] | $\geq 2$ |

Metallic mirrors will be used in LIR for the final steering of the laser onto the electron beam. The laser photons from the OL will reach the interaction region shown in fig. 6 and enter the LEP vacuum chamber through a quartz window $W_2$ to get the final deflection from the metallic mirror $M_6$. This will be introduced at the end of the LEP acceleration cycle and after the beam adjustments at the flat top so that the beam-to-mirror clearance can be reduced to $\approx 10$ mm ($\approx 26\ \sigma_y$, table 2). A second mirror $M_6'$ will recuperate the laser light after the interaction as discussed in section 4.

### 7.3. Collision angle and laser spot size

The collision angle should be chosen to maximize the luminosity of the interaction for a given laser pulse length. The necessity of having a small crossing angle to produce a long interaction region has to be balanced with the importance of reducing the sensitivity to vertical orbit misalignments. Interactions at very small angles are moreover limited by the position of the last mirror relative to the electron beam, which is in turn defined by the mirror dimensions and hence by the laser spot size at the interaction, for a given emittance of the laser beam.

The influence of the laser spot size on the luminosity has been studied for two three-dimensional Gaussian distributions crossing at an angle $2\delta_0$ using the notations in [35]. If the $\beta$ functions at the interaction are not too small the beam widths can be considered to be constant and the interaction area $\Sigma$ of eq. (5) is given by

$$\Sigma = \left\{2\pi\left[\left(\sigma_x^2+\sigma_{\phi x}^2\right)\left[\left(\sigma_y^2+\sigma_{\phi y}^2\right)\cos^2\delta_0 + \left(\sigma_z^2+\sigma_{\phi z}^2\right)\sin^2\delta_0\right]\right]^{1/2}\right\}\{\cos\ \delta_0\}^{-1}, \qquad (17)$$

where $\sigma_{x,y,z}$ and $\sigma_{\phi x,\phi y,\phi z}$ are the rms dimensions of the electron bunch and of the laser beam. Calculations have been performed varying the transverse dimensions $\sigma_\phi = \sigma_{\phi x} = \sigma_{\phi y}$ of a round laser beam colliding with an electron bunch of dimensions as from table 2. A laser pulse

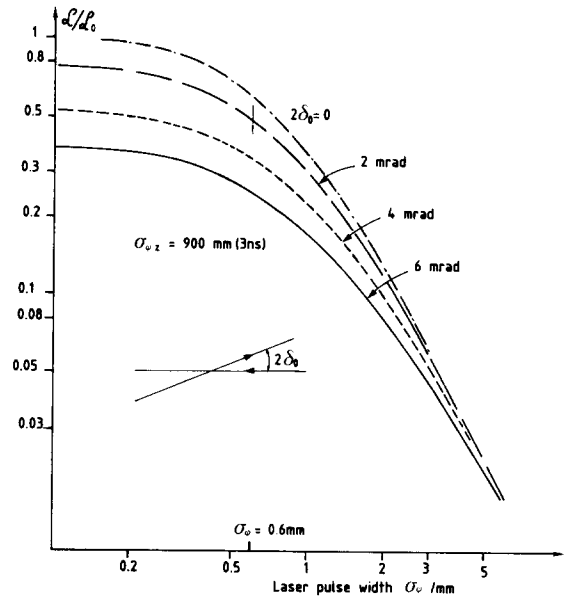


Fig. 10. Luminosity at LIR vs round laser beam width.

rms duration $\sigma_{\phi z} \approx 0.9$ m (3 ns) * and an electron bunchlength $\sigma_z = 15.8$ mm [36] have been assumed.

The relative luminosity is shown in fig. 10 as a function of the laser spot size at the interaction for collision angles $2\delta_0 = 2$, 4 and 6 mrad. Requiring a 10 mm clearance between the beam and the edge of the mirror $M_6$ and taking into account the laser beam emittance (table 4), a 2 mrad collision angle can be obtained with a nominal rms laser spot size at LIR

$$\sigma_\phi^* = 0.6 \text{ mm}. \qquad (18)$$

A smaller value of $\sigma_\phi^*$ would imply an increase of the interaction angle to accommodate the larger mirror dimensions and the 10 mm clearance, with no net advantage in the luminosity.

### 7.4. The laser beam transport line

The layout of the $\approx 127$ m long laser beam transport line is shown in fig. 11. After traversing an optical section for the generation and the control of the circular polarization, the laser light is deflected into separate beams when requested to illuminate either $e^+$ or $e^-$, reaches the tunnel through the mirrors $M_1$, $M_2$ and is directed towards the LIR through mirror $M_3$. A double 90° system (mirrors $M_4$ and $M_5$) provides the final alignment of the light on the last mirror $M_6$ in the special vacuum insertion. The mirror $M_6'$ would collect the light after the interaction for "remote polarimetry"

* The required laser technical specifications are collected in table 4.

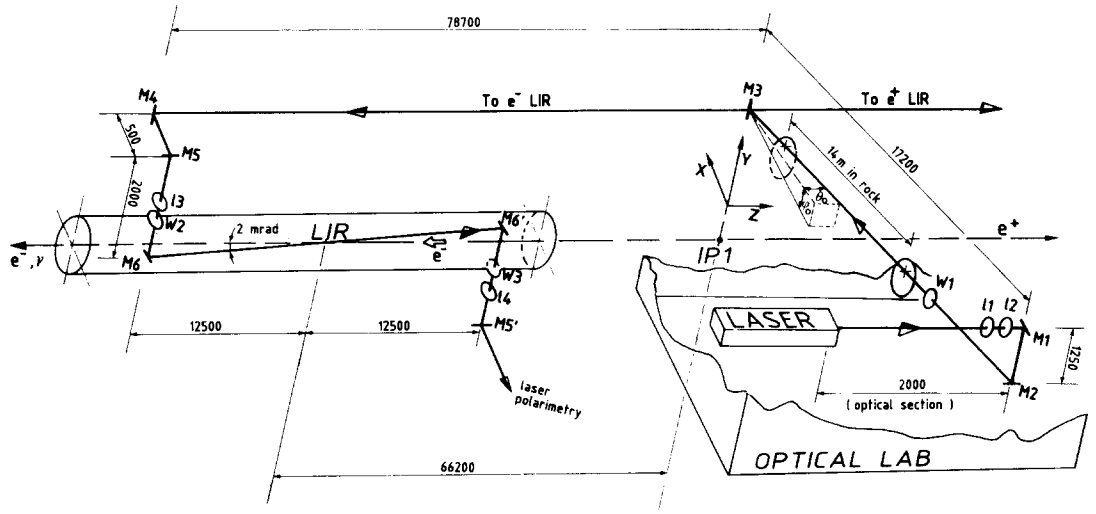


Fig. 11. Geometry of the laser beam transport line. Deflections at mirrors:

$M_1$: 90° $M_3$: 103°42′ ($e^-$), 76° 18′ ($e^+$) $M_5$: 90°

$M_2$: 103°26′ $M_4$: 90° $M_6$: 90° − 2 mrad = 89°53′08″.

$\vartheta_0 = 13°42'$ $\phi_0 = 13°26'$.

as discussed in section 4.3 or refocus it back to the optical laboratory. A proper combination of mirrors would assure the preservation of the photons circular polarization.

The transport optics sketched in fig. 12 images, over a distance of about 100 mm, the beam size at the end of the optical section in the OL to a focusing system ($f = 10.3$ m) located before the quartz window $W_2$ at the vacuum insertion, without any optical element in the LEP tunnel. The optical requirements for the laser final focus at LIR are defined by the considerations of section 7.3 on the nominal rms size $\sigma_\phi^*$ at the collision point.

For a laser operating in a $TEM_{00}$ mode the diameter of a Gaussian beam is defined as the width at $\pm 2\sigma$, i.e. at $1/e^2$ of the maximum irradiance [37]. The nominal laser spot size at LIR is then

$$4\sigma_\phi^* = 2.4 \text{ mm}. \tag{19}$$

This value is larger than the "diffraction limited" one, which in our case is

$$2r_{\min} = 3.25 f \lambda_\phi / D_{\text{opt}} \approx 0.4 \text{ mm}, \tag{20}$$

where $D_{\text{opt}}$ is the aperture of the focusing system and $\lambda_\phi$ the photon wavelength in μm (section 8). The unitary transport between the two optical systems allows the

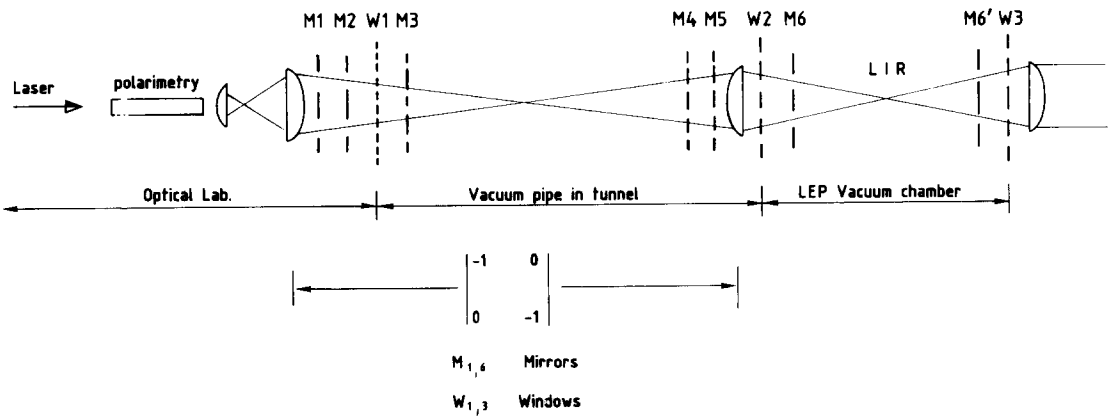


Fig. 12. Optics of the laser beam transport line.

Table 4
Laser technical specifications. Laser type: Nd:YAG Quantel COMPAC – YG661S longitudinal monomode

| | | |
|---|---|---|
| Wavelength [nm] | | 523 |
| Photon energy [eV] | | 2.33 |
| Repetition rate [Hz] | 10 | 30 |
| Peak power [MW] | 50 | 30 |
| Pulse length (FWHM) [ns] | 5–6 | 6–7 |
| Pulse energy [mJ/pulse] | 300 | 190 |
| Peak intensity [$10^{18}$ ph/pulse] | $\approx 0.8$ | $\approx 0.5$ |
| CW power [W] | 3 | 5.7 |
| Time jitter (rms) [ns] | 0.25 | 0.3 |
| Output emittance ($\sigma\sigma'$) [$\mu$m] | 0.3 | 0.4 |
| Output cavity beam diameter ($4\sigma$) [mm] | 6 | 6 |
| Full angle divergence ($4\sigma'$) [mrad] | 0.8 | 1 |

laser beam size at the LIR to be controlled from the OL. The laser spot (19) can, if desired, be increased up to a factor of 3 for easier beam finding during the commissioning of the polarimeter.

The parameters of the laser beam optics at LIR are collected in table 3. The maximum values for the beam dimensions and divergences refer to a laser emittance of 0.4 $\mu$m (table 4).

## 8. The laser parameters

Single and multiphoton techniques have been compared in section 5. The latter has been chosen since it provides a signal-to-background ratio per interaction considerably better than the former, which would be completely spoiled by synchrotron radiation even with the adopted layout. The adoption of the multiphoton technique implies the use of high peak power, low pulse-energy lasers (50 ÷ 100 MW, $\approx$ 500 mJ/pulse).

### *8.1. The laser beam wavelength* $\lambda_\phi$

The asymmetry (7) has a maximum around a rest frame scattering angle $\vartheta' \approx 90°$ where the function $F(\vartheta', k_0')$ reads:

$$F^* \equiv F(\vartheta' = 90°) = \frac{k_0'}{1 + k_0' + k_0'^2}. \tag{21}$$

The maximum of eq. (21) for $k_0' = 1$ states a relationship between the laser energy $E_\phi$ and the beam energy $E$ for optimum asymmetry condition

$$E_\phi E = 1.3 \times 10^{-7}\ \mathrm{GeV}^2, \tag{22}$$

which, for energies around 50 geV, prescribes the use of a laser in the visible range ($E_\phi \approx 2.6$ eV). From the definition (9) for $k_0'$ and introducing the relation

$$E_\phi \lambda_\phi = 1.24\ \mathrm{eV}\,\mu\mathrm{m} \tag{23}$$

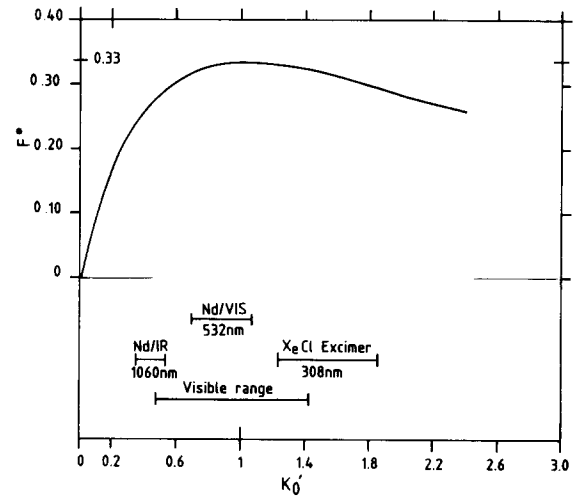


Fig. 13. Maximum asymmetry $F^*$ as a function of laser wavelength.

the function $F^*$ can be evaluated for various laser wavelengths. Figs. 13 and 14 show that in the LEP energy range lasers operating in the visible region provide maximum asymmetry.

A Nd-YAG laser operating on the fundamental frequency ($\lambda_\phi = 1.06$ $\mu$m) or an excimer laser (XeCl, $\lambda_\phi = 0.308$ $\mu$m) would produce a slightly reduced asymmetry while a 10.6 $\mu$m $CO_2$ laser provides a much smaller one.

Excimer lasers with 20 MW peak power at $\lambda_\phi = 0.308$ $\mu$m up to 250 Hz repetition rate are at present commercially available. The higher repetition rate would certainly constitute an advantage provided the associated average power can be handled by the optical system. Drawbacks are cost, a more complex structure including toxic gas manipulation (XeCl, KrCl or KrF) and the need for quartz lenses due to the shorter wavelength. Nd-YAG lasers with 50 ÷ 100 MW peak power at 0.532 and 1.06 $\mu$m are commercially available; their repetition rate is in the range of 10 ÷ 50 Hz due to the solid state

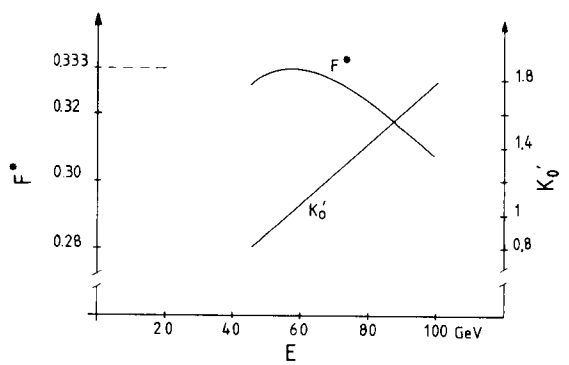


Fig. 14. Maximum asymmetry $F^*$ in the LEP energy range.

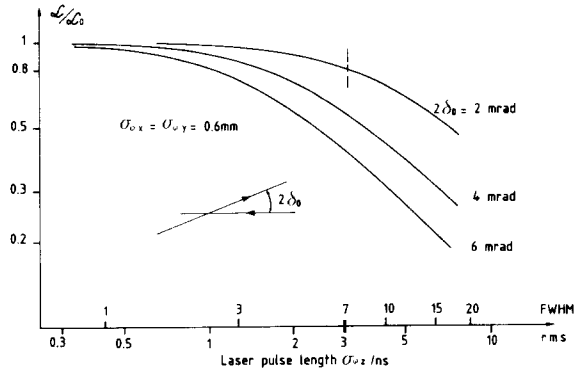


Fig. 15. Luminosity at LIR vs laser pulse length.

structure. Both devices can produce pulse durations in the range 5 to 8 ns. More reasonable costs and wider experience at DESY and SLAC with Nd-YAG lasers are not negligible advantages. In conclusion, a laser operating in the multiphoton regime (50 to 100 MW peak) and in the visible range (e.g. frequency doubled mode Nd-YAG, $\lambda_\phi = 532$ nm) represents our preferred proposal.

### 8.2. *The laser pulse duration* $\sigma_{\phi z}$

The luminosity from two Gaussian distributions intersecting at an angle $2\delta_0$ depends on the longitudinal rms sizes of the interacting bunches [eq. (17)]. In our case the dependence of the luminosity on the laser pulse duration has been investigated for the interaction with an electron bunch with the characteristics specified in section 7.3. The results are illustrated in fig. 15 where the luminosity for crossing angles $2\delta_0 = 2$, 4 and 6 mrad is shown as a function of $\sigma_{\phi z}$. A 2 mrad collision angle and an rms pulse length of 3 ns imply a $\approx 20\%$ reduction in the relative luminosity. The laser pulse duration should be chosen to be $\leq 3$ ns rms (7 ns FWHM) to

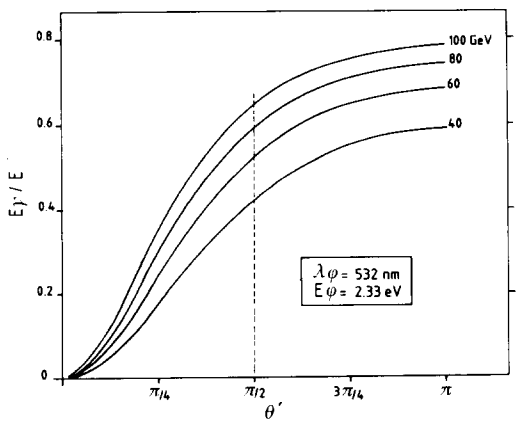


Fig. 16. Energy spectrum of the backscattered γ-beam.

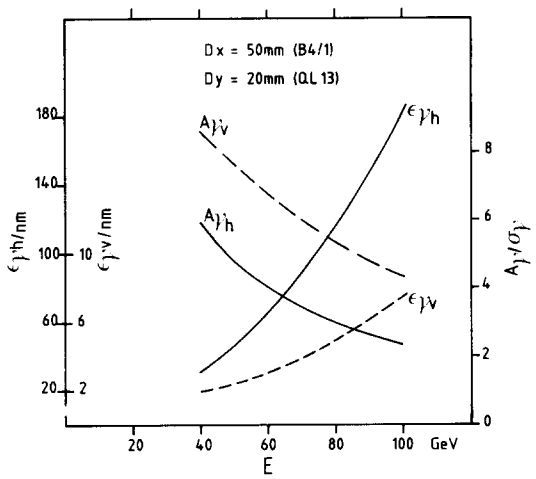


Fig. 17. Energy dependence of the γ-beam emittances and of the γ-channel acceptances.

keep the reduction in the luminosity within reasonable limits. Possible laser parameters are collected in table 4.

## 9. The recoil γ-beam

### 9.1. *Energy spectrum*

The relative energy distribution of the backscattered γ-beam, $E_\gamma/E$, is a function of the laser energy $E_\phi$ [eq. (9) and (B.4)]:

$$E_\gamma/E \equiv |k|/\gamma \approx \frac{2\gamma k_0(1-\cos\vartheta')}{1+k_0'(1-\cos\vartheta')}. \qquad (24)$$

The ratio $E_\gamma/E$ has been computed as a function of the angle $\vartheta'$ for several LEP energies for a 2.33 eV (532 nm) laser light. The results of fig. 16 show that in the range $\vartheta' = 90° \div 180°$ the backscattered γ-beam energy is in the range 15 to 40 GeV for LEP I ($E = 46$–$60$ GeV).

### 9.2. *Apertures and diaphragms*

The transmission of the Compton backscattered γ's to the detector is limited by the available apertures on the line of flight (fig. 7). The diaphragms are essentially located in the modified vacuum chamber inside the B4/1 dipole (horizontal diaphragm $D_x = 50$ mm) and between the external coils of the quadrupole QL14 (vertical diaphragm $D_y = 20$ mm).

To evaluate the acceptance of the γ-beam channel an "equivalent emittance" of the photon beam has been derived from that of the electron beam at the illumination point (table 2) by quadratically adding the contribution to the divergence from the Compton scattering. Using the standard beam optics notations and recalling

Table 5
γ-beam dimensions at diaphragms and detector for $E = 46$, 60 and 100 GeV

| Position (m) | Distance from LIR (m) | $\sigma_{\gamma x}$ (mm) | $\sigma_{\gamma y}$ (mm) | Diaphragm (mm) |
|---|---|---|---|---|
| Mid B4/1 | 220.6 | 9.5 | 2.3 | 50 ($D_x$) |
| | | 12.5 | 2.7 | |
| | | 20.8 | 4.2 | |
| Out QL13 | 235.6 | 10.2 | 2.5 | 20 ($D_y$) |
| | | 13.4 | 2.9 | |
| | | 22.2 | 4.6 | |
| Detector | ≈ 275 | 11.8 | 2.9 | |
| | | 15.6 | 3.5 | |
| | | 25.8 | 5.5 | |

eq. (B.2) for the scattering angle $\vartheta$ in the laboratory the equivalent γ-beam emittance at the illumination point

$$\epsilon_\gamma \approx \left[\sigma_\gamma \sigma'_\gamma/(1+\alpha^2)\right]_{\text{ill.point}} \tag{25}$$

with

$$\sigma_\gamma = \sigma \quad \text{and} \quad \sigma'_\gamma = \sqrt{(\vartheta^2 + \sigma'^2)} \approx \sqrt{(\gamma^{-2} + \sigma'^2)} \tag{26}$$

has been evaluated in both planes from the beam parameters $\sigma$, $\sigma'$ of Table 2.

The γ-beam dimensions at the diaphragms and at the detector, computed introducing the local $\beta$-functions (drift space transformation), are collected in table 5 for $E = 46$, 60 and 100 GeV.

The following conclusions can be derived for
1) The aperture of the γ-beam transport line in the energy range 46–60 (100) GeV:

$$\begin{aligned} A_{\gamma x} &= [5.3\text{–}4.0\ (2.4)]\,\sigma_{\gamma x} \quad (D_x = 50\ \text{mm}), \\ A_{\gamma y} &= [8.1\text{–}6.8\ (4.4)]\,\sigma_{\gamma y} \quad (D_y = 20\ \text{mm}). \end{aligned} \tag{27}$$

2) The minimum required sensitive area of the detector:

$$S_{\text{det}} \geq 63\ \text{mm} \times 24\ \text{mm}(X \times Y). \tag{28}$$

The emittances $\epsilon_{\gamma x,y}$ together with the transmission $(A/\sigma)_{\gamma x,y}$ of the γ-channel are shown as a function of energy in fig. 17.

### 9.3. *Accuracy for the orbit control at LIR*

A tight control fo the closed orbit at the LIR is mandatory to match the γ-beam to the above discussed physical apertures and to the γ-detector. The transmission efficiency and the position of the γ-beam at the detector can be affected by different sources of error.

#### 9.3.1. *Setting accuracy of correcting dipoles*

The residual kick produced by an uncertainty $\Delta \int B\,\mathrm{d}s$ [Gm] on the corrector field is

$$\delta\theta = 30\frac{\Delta \int B\ \mathrm{d}s}{E}[\mu\text{rad}]. \tag{29}$$

The ≈ 1 Gm setting accuracy o the LEP orbit correctors [38], which corresponds to a kick error $\delta\theta$ of about 0.7 μrad and an offset at the detector of about 0.2 mm at 46 GeV, seems adequate.

#### 9.3.2. *Position error at the pickups near to the LIR*

Assuming an uncertainty of ±0.3 mm on the absolute position of the electron beam measured by the pickups at quadrupoles QL2, QL4 and QL5 (≈ 80 m basis) the residual maximum error of ≈ 7.5 μrad on the slope of the closed orbit at LIR results in an offset at the detector of about 2 mm and a 10% reduction of the vertical acceptance (section 9.2).

#### 9.3.3. *Long term closed orbit drift*

The closed orbit at LIR can be affected by long term drifts with amplitudes smaller than the resolution of the beam position monitors in LSS1. Due to the distance to the detector, this could spoil the measurement of the asymmetry.

The detector described in the next paragraph has been conceived to help in compensating the last two effects.

## 10. Considerations on the γ-detector

A very compact high density tungsten/silicon detector will resolve the small vertical asymmetry of the backscattered γ's. The sandwich-like structure, derived from the solution adopted for the Bhabha relative luminosity monitors [39], is composed of two vertical silicon double half-planes separated by a 2 r.l. tungsten converter. A first ≈ 6 r.l. tungsten layer will let the γ-shower develop while filtering out most of the synchrotron radiation flux. Two silicon strip planes * will allow to record the profiles of the recoil γ-beam in both planes (fig. 18).

A W–Si calorimeter [40] with only two sensitive planes has a resolution of $\approx 125\%/\sqrt{E}$. At an average γ energy of about 25 geV this resolution amounts to ≈ 25% and will contribute by only 6% to the statistical fluctuations when a bunch of γ's are recorded.

The detector has a horizontal symmetry plane and allows for simultaneous recording of the backscattered γ's above and below the center of gravity of their vertical distributions (fig. 8). The number of counts $n_{\text{Ru}} + n_{\text{Lu}}$ and $n_{\text{Rd}} + n_{\text{Ld}}$ recorded in the upper and the

* 32 mm/16 channels covering ±6 σ's of the γ-distributions at the detector.

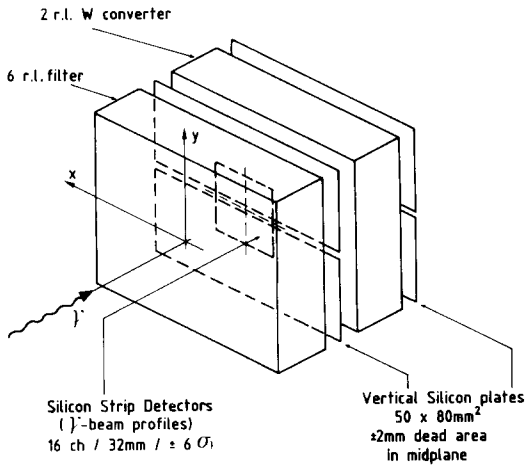


Fig. 18. Schematic of the γ-detector layout.

lower halves of the detector for both photon helicities can be combined to give the asymmetry

$$A = \frac{n_{\mathrm{Ru}} - n_{\mathrm{Lu}} + n_{\mathrm{Ld}} - n_{\mathrm{Rd}}}{n_{\mathrm{Ru}} + n_{\mathrm{Lu}} + n_{\mathrm{Ld}} + n_{\mathrm{Rd}}}. \tag{30}$$

The asymmetry (30) is insensitive to systematic errors originating from drifts in the closed orbit at LIR. An analogous algorithm can be set up to monitor any sistematic vertical offset at the detector, and this information will be used for a position feedback. The asymmetry method is sensitive to systematic effects from changes in the vertical electron beam size at the LIR. The related uncertainty in the polarization measurement can be eliminated by a normalization of the asymmetry to the measured rms dimensions of the recoil gamma beam. The analyzing power of the polarimeter, evaluated with the code ASYM for $E = 46$ GeV and the $e^-$ beam parameters of table 2, is

$$\Pi(P_\phi = 1) = \frac{\partial A}{\partial P_e} \approx 11.3\%. \tag{31}$$

## 11. Rates, accuracies and measuring time

The adoption of the multiphoton technique and the availability of a laser fulfilling the recommendations of section 8 would provide a backscattered γ-rate

$$r_\gamma \approx (1\text{–}3) \times 10^5 \text{ Hz}. \tag{32}$$

The relative statistical accuracy $\delta A/A$ for the asymmetry (30) is a function of $A$:

$$\frac{\delta A}{A} \approx \frac{1}{A\sqrt{2\langle n_{\mathrm{R,L}}\rangle}}, \tag{33}$$

where $\langle n_{\mathrm{R,L}}\rangle$ is the average number of counts at each photon helicity required for a given accuracy. Introducing the analyzing power (31) the measuring time in terms of the polarization level $P_e$ and the statistical accuracy $\delta A/A$ is

$$T_{\mathrm{meas}} = \frac{\langle n_{\mathrm{R,L}}\rangle}{r_\gamma} \approx \frac{1}{2r_\gamma[\Pi P_e(\delta A/A)]^2}\,[\mathrm{s}] \tag{34}$$

The measuring time $T_{\mathrm{meas}}$ is shown in fig. 19 as a function of $P_e$ for different accuracies $\delta A/A$. Numerical estimates are given in table 6 for $r_\gamma = 2 \times 10^5$ Hz.

Table 6
Measuring time as a function of $P_e$ and $\delta A/A$

| $P_e$ (%) | $A$ (%) | $\delta A/A$ (%) | $T_{\mathrm{meas}}$ (s) |
|---|---|---|---|
| 70 | 7.9 | 3 | 0.5 |
| | | 10 | 0.05 |
| 50 | 5.6 | 3 | 1 |
| | | 10 | 0.1 |
| 10 | 1.1 | 3 | 20 |
| | | 10 | 2 |

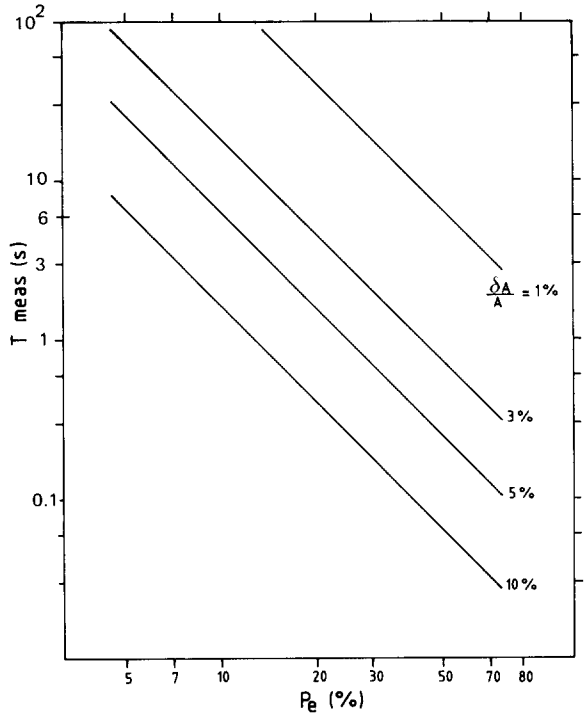


Fig. 19. Measuring time as a function of the electron polarization level $P_e$. $\Pi = 0.113$, $P_\phi = 1$.

## 12. Conclusions

A detailed study of the LEP transverse polarimeter showing attractive performance has been presented and suggests the following remarks:

- The choice of a layout avoiding synchrotron radiation from the main dipoles and the adoption of the

multiphoton method provide a favourable signal to noise ratio in the measurement of the asymmetry.
- Laser specifications fulfilling the multiphoton requirements have been defined. They can be met by commercially available devices.
- The optimization of the laser beam optics and specifically of the interaction geometry appears to provide promising performance.
- When LEP is operated at an energy of $\approx 55$ GeV with the existing wigglers, the polarimeter is powerful enough to monitor the polarization buildup at a rate of about 1% per minute.

**Acknowledgements**

We are indebted to C. Bovet, R. Jung, B.W. Montague and D. Plane, C. Prescott (SLAC), R. Schmidt (DESY) and J. Kewisch (CEBAF) for interesting discussions on the many aspects of the study. E. Picasso recounted for us the most recent experimental results on the electron and positron $g$ factors. Conversations with C. Bovet and A. Hofmann on the behavior of the luminosity for beams crossing at an angle have been of great help.

We would like to thank P. Gourber, O. Grobner and C. Wyss for advice on the implications deriving from the required modifications to the original LEP layout. The technical studies on the special vacuum chambers and insertions performed by C. Grunhagel under the coordination of J.C. Brunet constitute a precious contribution to the realization of this proposal. Thanks are due to T. Garvey for the careful reading of the text.

## Appendix A

*Short review of the Compton effect*

The cross section of the Compton effect in the electron restframe is calculated in ref. [23]. The kinematic notation is defined in fig. 1 where a photon of energy $k'_0$ hits an electron at rest and the scattered photon has energy $k'$, scattering angle $\vartheta'$ and azimuthal angle $\phi'$.

The energies $k$ and $k'$ are in units of electron rest mass. The Compton cross section is:

$$\mathrm{d}\sigma_c/\mathrm{d}\Omega = \left(r_0^2/2\right)\left(k'/k'_0\right)^2\left(\Phi_0 + \Phi_1 + \Phi_2\right), \qquad (A.1)$$

with

$$\Phi_0 = (1 + \cos^2\vartheta') + (k'_0 - k')(1 - \cos\vartheta'),$$

$$\Phi_1 = \xi_1 \sin^2\vartheta',$$

$$\Phi_2 = -\xi_3(1 - \cos\vartheta')\boldsymbol{\zeta}\cdot(\boldsymbol{k}'_0\cos\vartheta' + \boldsymbol{k}'),$$

$r_0 = e^2/m_e c^2$ (classical electron radius),

$\boldsymbol{\zeta} \equiv (\zeta_1, \zeta_2, \zeta_3)$ = electron polarization vector,

$\boldsymbol{\xi} \equiv (\xi_1, \xi_2, \xi_3)$ = light polarization vector.

For any arbitrary polarized plane wave composed by two orthogonal waves:

$$E_x = a_x \exp[\mathrm{i}(kz - \omega t + \psi_1)],$$

$$E_y = a_y \exp[\mathrm{i}(kz - \omega t + \psi_2)],$$

the light polarization is described by the three-dimensional vector $\boldsymbol{\xi}$

$$\xi_1 = a_x^2 - a_y^2,$$

$$\xi_2 = 2a_x a_y \cos(\psi_1 - \psi_2),$$

$$\xi_3 = 2a_x a_y \sin(\psi_1 - \psi_2).$$

The cross section (A.1) depends on the electron polarization through the spin-dependent term $\Phi_2$. For vertical electron polarization $[\boldsymbol{\zeta} \equiv (0, 0, \pm P_e)]$ and circularly polarized light $[\boldsymbol{\xi} \equiv (0, 0, \pm P_\phi)]$:

$$\Phi_2 = \pm P_e P_\phi \cos\phi'(1 - \cos\vartheta')\, k' \sin\vartheta'. \qquad (A.2)$$

The maximum difference is for $\phi' = 0°$ or $180°$ and an angle $\vartheta' = 90°$.

## Appendix B

*Kinematics*

Energy/momentum conservation:

$$1/k' - 1/k'_0 = 1 - \cos\vartheta', \qquad (B.1)$$

scattering angles:

$$\gamma\vartheta \approx \sin\vartheta'/(1 - \cos\vartheta') = \cot(\vartheta'/2) \leq 1, \qquad (B.2)$$

incoming photon energies:

$$k'_0/\gamma k_0 = 1 + \cos\vartheta \approx 2, \qquad (B.3)$$

scattered photon energies:

$$k \approx \gamma k'(\cos\vartheta' - 1)$$

$$\approx 2\gamma^2 k_0(\cos\vartheta' - 1)/[1 + k'_0(1 - \cos\vartheta')]. \qquad (B.4)$$

## References

[1] B.W. Montague, CERN/LEP-TH/86-19 (Sept. 1986).
[2] B.W. Montague, Conference on High Energy Physics with Polarized Beams and Targets (178) AIP Conf. Proc. No. 51.
[3] B.W. Montague, Nucl. Instr. and Meth. 192 (1982) 165.
[4] C. Bovet, B.W. Montague, M. Placidi and R. Rossmanith, IEEE Trans. NS-32 (5) (Oct. 1985) 1911 (1985 Particle Accelerator Conference, Vancouver).
[5] M. Placidi and R. Rossmanith, LEP Note 539 (July 1985).

[6] G. Alexander et al., Report on the Polarimetry Working Group, Proc. Workshop on Polarization at LEP, to be published at CERN (1988).
[7] A.A. Sokolov and I.M. Ternov, Sov. Phys. Dokl. 8 (1964) 1203.
[8] R.F. Schwitters, Conference on High Energy Physics with Polarized Beams and Targets (1978) AIP Conf. Proc. No. 51.
[9] J.M. Paterson, J.R. Rees and H. Wiedemann, SPEAR-186/PEP-125 (1975).
[10] A. Hutton, Particle Accelerators 7 (1976) 177.
[11] A.M. Kondratenko and B.W. Montague, CERN/ISR-TH/80-38 (1980).
[12] B.W. Montague, Physics Reports 113 (1) (Nov. 1984).
[13] J.M. Jowett and T.M. Taylor, IEEE Trans. NS-30 (1983) 2581 (1983 Particle Accelerator Conference, Santa Fe).
[14] G. Guignard, J.M. Jowett and T.M. Taylor, LEP Note 521 (Nov. 1984).
[15] A. Blondel and J.M. Jowett, LEP Note 606 (May 1988).
[16] V.N. Baier and V.A. Khoze, Sov. J. Nucl. Phys. 9 (1969) 238.
[17] D.B. Gustavson et al., Nucl. Instr. and Meth. 165 (1979) 177.
[18] H.C. Dehne et al., Conference on High Energy Physics with polarized Beams and Targets (1978) AIP Conf. Proc. No. 51.
[19] A.S. Artomonov et al., Phys. Lett. 118B (1982) 498.
[20] D.B. Barber et al., Phys. Lett. 135B (1984) 498.
[21] W.W. Mackay et al., Phys. Rev. D29 (1984) 2485.
[22] D. Blockus et al., Proposal for Polarization at the SLC (April 1986).
[23] F.W. Lipps and H.A. Toelhoek, Polarization Phenomena of Electrons and Photons, Physica 20 (1954) 85, 395.
[24] R. Neumann and R. Rossmanith, Nucl. Instr. and Meth. 204 (1982) 29.
[25] R.S. Van Dyck Jr. et al., Phys. Rev. Lett. 59 (1987) 26.
[26] D.P. Barber et al., IEEE Trans. Nucl. Sci., NS-30 (1983) 2710.
[27] H.D. Bremer et al., DESY 82-026 (May 1982).
[28] H.W. Koch and J.W. Motz, Rev. Mod. Phys. 31 (1959) 920.
[29] J.H. Hubbell, Atomic Data 3 (1971) 241–297.
[30] U. Scholz, DESY Int. Ber. PET-78/03 (1978).
[31] C. Bovet and M. Placidi, LEP Note 532 (April 1985).
[32] Ph. Lebrun, J. Phys. (Paris) Cl T45 (1984).
[33] R. Schmidt, DESY M-82-22 (1982).
[34] F. Zwack, DESY M-85-03 (1985).
[35] T. Suzuki, KEK-76-3 (July 1976).
[36] LEP Design Report-CERN-LEP/84-01 (June 1984).
[37] C.B. Hitz, Understanding Lasers, (Penn Well Books, 1985).
[38] G. Guignard, LEP Note 403 (Aug. 1982).
[39] J.Y. Hemery, F. Lemeilleur and G. von Holtey, CERN/LEP-B1/86-6.
[40] G. Barbiellini et al., Nucl Instr. and Meth. A235 (1985) 55-60.